# Nuclear pasta in hot and dense matter and its influence on the equation of state for astrophysical simulations

Fan Ji [1], Jinniu Hu [1,2,*], Shishao Bao [3,†] and Hong Shen [1,‡]

[1]*School of Physics, Nankai University, Tianjin 300071, China*
[2]*Strangeness Nuclear Physics Laboratory, RIKEN Nishina Center, Wako 351-0198, Japan*
[3]*School of Physics and Information Engineering, Shanxi Normal University, Linfen 041004, China*

We explore the properties of nuclear pasta appearing in supernova matter, i.e., matter at finite temperature with a fixed proton fraction. The pasta phases with a series of geometric shapes are studied using the compressible liquid-drop (CLD) model, where nuclear matter separates into a dense liquid phase of nucleons and a dilute gas phase of nucleons and α particles. The equilibrium conditions for two coexisting phases are derived by minimization of the total free energy including the surface and Coulomb contributions, which are clearly different from the Gibbs conditions for phase equilibrium due to the finite-size effects. Compared to the results considering only spherical nuclei, the inclusion of pasta phases can delay the transition to uniform matter and enlarge the region of nonuniform matter in the phase diagram. The thermodynamic quantities obtained in the present calculation with the CLD model are consistent with those in the realistic equation of state table for astrophysical simulations using the Thomas-Fermi approximation. It is found that the density ranges of various pasta shapes depend on both the temperature T and the proton fraction Y_p. Furthermore, the nuclear symmetry energy and its density dependence may play crucial roles in determining the properties of pasta phases. Our results suggest that the pasta phase diagram is most sensitively dependent on the symmetry energy slope L especially in the low-Y_p and high-T region.

I. INTRODUCTION

Core-collapse supernovas are one of the most fascinating phenomena in the universe, and lead to the formation of neutron stars or black holes. During the past decades, great efforts have been devoted to numerical simulations of gravitational collapse of massive stars [1–3], in which the equation of state (EOS) of dense matter is an essential ingredient. The EOS plays an important role in understanding the dynamics of supernova explosions, which requires information over very wide ranges of temperature, proton fraction, and baryon density (see, e.g., Table 1 of Ref. [4]). In the full thermodynamic parameter space, the nuclear matter exhibits a rich and complex phase diagram. At low temperatures and subsaturation densities, the matter is nonuniform where heavy nuclei are formed to lower the free energy of the system. When the density is beyond $\approx 1/2$ nuclear saturation density, heavy nuclear clusters tend to dissolve into a uniform nucleon liquid. It is likely that nonspherical nuclei, known as pasta phases, may appear as the density approaches the phase transition to uniform matter [5–9]. However, heavy nuclei cannot be formed above a critical temperature, where the matter is a mixture of free nucleons and light clusters together with leptons [10,11]. At densities much higher than nuclear saturation density, non-nucleonic degrees of freedom like hyperons and quarks may occur and soften the EOS of dense matter [12].

It is a challenge to construct a realistic EOS covering the whole range of thermodynamic conditions for numerical simulations of core-collapse supernovas. Currently, there are various EOSs available for astrophysical simulations such as core-collapse supernovas and neutron-star mergers (see, e.g., Ref. [12] for a recent review). One of the most commonly used EOSs is the Lattimer-Swesty EOS [13], which employed a compressible liquid-drop (CLD) model with Skyrme forces to describe heavy nuclei in nonuniform matter. Recently, the approach of Lattimer and Swesty was extended and improved by Schneider *et al.* [14,15] for computing many EOSs based on Skyrme-type parametrizations of the nuclear forces. Another commonly used EOS is often referred to as the Shen EOS [4,16,17], which was based on the relativistic mean-field (RMF) model and Thomas-Fermi approximation with a parametrized nucleon distribution for the description of nonuniform matter. A similar Thomas-Fermi approximation with realistic nuclear forces was used to construct the EOS table by Togashi *et al.* [18] recently. In these realistic EOSs for astrophysical simulations, the nonuniform matter at intermediate densities is treated using the single nucleus approximation (SNA) [19]. There are also several EOSs that were developed beyond the SNA by including multiple nuclei in the framework of nuclear statistical equilibrium (NSE) [20–24].

---

*hujinniu@nankai.edu.cn
†bao_shishao@163.com
‡shennankai@gmail.com

Usually only spherical heavy nuclei are considered in constructing the EOS tables. In the present work, we intend to explore the influence of nonspherical pasta phases on the EOS for astrophysical simulations.

The appearance of nuclear pasta is mainly caused by the competition between the surface and Coulomb energies of heavy nuclei. As a result, the stable nuclear shape in nonuniform matter may change from droplet to rod, slab, tube, and bubble with increasing baryon density. Nuclear pasta phases are expected to occur both in core-collapse supernova matter with fixed proton fraction at finite temperature and in the inner crust of neutron stars where neutron-rich matter is in β equilibrium at zero temperature. Over the past decades, the properties of pasta phases have been studied using various methods, such as the liquid-drop model [25–28] and the Thomas-Fermi approximation [6,29–31]. Generally, the Wigner-Seitz approximation with typical geometric shapes of nuclear pasta is employed to simplify the calculations. For more realistic description, there are some studies that have not explicitly assumed any geometric shape and performed fully three-dimensional calculations for nuclear pasta based on the Thomas-Fermi approximation [8,32,33], Hartree-Fock approach [5,11,34–37], and molecular dynamics method [7,38–42]. It is noteworthy that nuclear symmetry energy and its slope could significantly affect the pasta phase structure and crust-core transition of neutron stars [9,29,30].

For the pasta phases in supernova matter, Pais *et al.* [31] performed calculations and compared results using three different methods: the coexisting phases (CP) method, the CLD model, and the self-consistent Thomas-Fermi approximation. The CP method is relatively simple, whereby two coexisting phases satisfy the Gibbs conditions for phase equilibrium, whereas the surface and Coulomb contributions are perturbatively taken into account [6,43]. In the CLD model, the surface and Coulomb contributions are treated in a more consistent manner, and are included in the minimization procedure and lead to some additional terms in the equilibrium conditions [44]. The Thomas-Fermi approximation describes the nucleon distributions of pasta phases in a realistic way, whereby the finite-size effects are treated self-consistently. Recently, the impact of nuclear pasta on the neutrino scattering rates has been discussed for core-collapse supernovas and protoneutron star evolution [45,46], and it was found that the presence of nuclear pasta could alter the late-time neutrino signal from supernovas. The elastic properties of nuclear pasta are presently interesting to some researchers for their relevance to gravitational wave searches both from supernova and neutron-star mergers, which motivates calculations of the pasta phase diagram [47–50]. Therefore, it is interesting and important to investigate under which conditions the pasta phases can occur.

In this article, we have two aims. The first is to investigate the properties of pasta phases that occur in supernova matter, while the effects of nuclear symmetry energy are examined by using two RMF models, namely, the TM1 and TM1e parametrizations [44,51], which have the same properties of symmetric nuclear matter but different behaviors of the symmetry energy. The second is to explore the influence of nuclear pasta on the EOS for astrophysical simulations. We perform calculations of nonuniform matter using the CLD model, where a nuclear liquid coexists with a dilute gas consisting of free nucleons and α particles employing a sharp interface. By comparing the results with and without pasta phases, we analyze the possible impact from nuclear pasta on the phase diagram and thermodynamic quantities. Since both the TM1 and TM1e models have been employed in constructing the EOS tables for core-collapse supernova simulations using a parametrized Thomas-Fermi approximation [4,52], it is possible to examine the difference between the present results using the CLD method and the values from realistic EOS tables, so that the uncertainty due to different descriptions of nonuniform matter can be estimated quantitatively.

It is necessary to check the nuclear model by recent developments in astrophysical observations. One strong constraint coming from the mass measurements of massive pulsars [53–56] requires the maximum neutron-star mass to be larger than $\approx 2M_\odot$. We notice that the TM1 and TM1e models predict maximum neutron-star masses of $2.18M_\odot$ and $2.12M_\odot$, respectively. Recently, the first detection of gravitational waves from a binary neutron-star merger, known as GW170817, provided valuable constraints on the tidal deformability [57,58], which also restricts the radius of a canonical $1.4M_\odot$ neutron star as $R_{1.4} < 13.8$ km [59–63]. More recently, the second detection of gravitational waves, GW190425, was reported by the LIGO and Virgo Collaborations [64]. The latest observations by the Neutron Star Interior Composition Explorer (NICER) for PSR J0030+0451 provided a simultaneous measurement of the mass and radius of a neutron star [65,66]. It is interesting to notice that constraints on the neutron-star radius from various observations are consistent with each other. In our previous work [67], we studied the correlation between the neutron-star radius and the slope parameter L of symmetry energy using a family of RMF models generated from the TM1 parametrization. The TM1e model with $L = 40$ MeV predicts a radius of $R_{1.4} = 13.1$ km that is well within the current constraints, whereas the original TM1 model with $L = 110.8$ MeV results in a much larger radius of $R_{1.4} = 14.2$ km. Furthermore, the neutron-star maximum mass and tidal deformability predicted by the TM1e model are also compatible with observational constraints. In the present study, we employ the TM1e model with $L = 40$ MeV to perform calculations of nonuniform matter including pasta phases, whereas the results from the original TM1 model with $L = 110.8$ are also presented to examine the influence of the density dependence of symmetry energy.

This article is organized as follows. In Sec. II, we briefly review the RMF model used and describe the CLD method for the description of pasta phases in hot and dense matter. In Sec. III, the results of nuclear pasta and its influence on the EOS are discussed. Finally, the conclusions are presented in Sec. IV.

II. FORMALISM

We study the nuclear pasta phases at finite temperature based on the CLD method, where the RMF model with extended TM1 parametrization is used for the nuclear

TABLE I. Coupling constants of the TM1e and TM1 models with symmetry energy E_{sym} and slope L at saturation density.

Model	E_{sym} (MeV)	L (MeV)	g_σ	g_ω	g_ρ	g_2 (fm^{-1})	g_3	c_3	Λ_{v}
TM1e	31.38	40	10.0289	12.6139	13.9714	−7.2325	0.6183	71.3075	0.0429
TM1	36.89	110.8	10.0289	12.6139	9.2644	−7.2325	0.6183	71.3075	0.0000

interaction [44]. In the RMF approach, nucleons interact via the exchange of various mesons including the isoscalar-scalar meson σ, isoscalar-vector meson ω, and isovector-vector meson ρ. The nucleonic Lagrangian density reads

$$
\begin{aligned}
\mathcal{L} = \sum_{i=p,n} \bar{\psi}_i & \left[i\gamma_\mu \partial^\mu - (M + g_\sigma \sigma) \right. \\
& \left. - \gamma_\mu \left(g_\omega \omega^\mu + \frac{g_\rho}{2} \tau_a \rho^{a\mu} \right) \right] \psi_i \\
& + \frac{1}{2} \partial_\mu \sigma \partial^\mu \sigma - \frac{1}{2} m_\sigma^2 \sigma^2 - \frac{1}{3} g_2 \sigma^3 - \frac{1}{4} g_3 \sigma^4 \\
& - \frac{1}{4} W_{\mu\nu} W^{\mu\nu} + \frac{1}{2} m_\omega^2 \omega_\mu \omega^\mu + \frac{1}{4} c_3 (\omega_\mu \omega^\mu)^2 \\
& - \frac{1}{4} R_{\mu\nu}^a R^{a\mu\nu} + \frac{1}{2} m_\rho^2 \rho_\mu^a \rho^{a\mu} \\
& + \Lambda_{\text{v}} \left(g_\omega^2 \omega_\mu \omega^\mu \right) \left(g_\rho^2 \rho_\mu^a \rho^{a\mu} \right),
\end{aligned}
\tag{1}
$$

where $W^{\mu\nu}$ and $R^{a\mu\nu}$ denote the antisymmetric field tensors for ω^μ and $\rho^{a\mu}$, respectively. Under the mean-field approximation, the meson fields are treated as classical fields and the field operators are replaced by their expectation values. In a static system, the nonvanishing expectation values of meson fields are $\sigma = \langle\sigma\rangle$, $\omega = \langle\omega^0\rangle$, and $\rho = \langle\rho^{30}\rangle$. From the Lagrangian density (1), we derive in the standard way the equations of motion for the nucleon and meson fields, which are coupled with each other and can be solved self-consistently. It is straightforward to obtain the expressions for the free energy density and pressure in uniform nuclear matter at finite temperature [68].

In the Lagrangian density (1), an ω-ρ coupling term (i.e., the last term) is introduced in addition to the original TM1 model. It is well known that ω-ρ coupling plays a crucial role in determining the density dependence of the symmetry energy [69–73]. By adjusting the coupling constants, g_ρ and Λ_{v}, it is possible to control the behavior of symmetry energy and its density dependence. In our previous work [44], we generated a set of RMF models, based on the TM1 parametrization, which have the same isoscalar properties and fixed symmetry energy at a density of 0.11 fm^{-3} but have different symmetry energy slope L. In the present study, we perform the calculations for pasta phases employing the extended TM1 model with $L = 40$ MeV, which is referred to as the TM1e model. It is found that the TM1e model provides satisfactory descriptions for both finite nuclei and neutron stars. To study the influence of symmetry energy slope L, the results of the TM1e model are compared to those of the original TM1 model with $L = 110.8$ MeV. For completeness, we present in Table I the coupling constants of the TM1e and TM1 models. It is shown that only g_ρ and Λ_{v} related to

isovector parts are different, while all other parameters remain the same. Therefore, the isoscalar saturation properties are the same between these two models, while the behaviors of symmetry energy are different. In the TM1e model, the symmetry energy and its slope parameter at saturation density are $E_{\text{sym}} = 31.38$ MeV and $L = 40$ MeV, which are well within the constraints from various observations [12]. The corresponding values in the original TM1 model are $E_{\text{sym}} = 36.89$ MeV and $L = 110.8$ MeV, which are considered to be rather large and disfavored by recent astrophysical observations.

To describe the pasta phases in hot and dense matter, we employ the CLD model [31,44,68], where the Wigner-Seitz approximation is adopted for simplifying the calculation of the free energy. The nuclear matter inside the Wigner-Seitz cell is assumed to separate into a dense liquid (L) phase and a dilute gas (G) phase by a sharp interface, while the background electron gas is approximated to be uniform with the density determined by the charge neutrality condition. In general, the possible geometric structure of pasta phases may change from droplet to rod, slab, tube, and bubble with increasing baryon density. At given temperature T, average baryon density n_b, and proton fraction Y_p, the equilibrium state can be determined by minimizing the total free energy density of the system among all configurations considered [4,13,44]. The free energy density of the pasta phases is expressed as

$$
\begin{aligned}
f = u f^L \left(n_p^L, n_n^L \right) & + (1-u) f^G \left(n_p^G, n_n^G, n_\alpha^G \right) \\
& + f_{\text{surf}}(u, r_D, \tau) + f_{\text{Coul}} \left(u, r_D, n_p^L, n_p^G, n_\alpha^G \right),
\end{aligned}
\tag{2}
$$

where u is the volume fraction of the liquid phase. The proton and neutron densities in the liquid (gas) phase are denoted by n_p^L (n_p^G) and n_n^L (n_n^G), respectively. The free energy contributed from nucleons in phase i ($i = L, G$) can be calculated in the RMF models [4,68]. Note that contributions from electrons are not included in Eq. (2), since the background electron gas with a fixed density plays no role in the minimization procedure. Generally, the contributions from leptons and photons are treated separately when one constructs the EOS table for astrophysical simulations. At finite temperature, the α particle may exist as a representative light nucleus in the dilute gas phase, whereas it is absent in the dense liquid phase. This is because the α particle tends to dissolve close to nuclear saturation density due to the finite volume effect [4,13]. For simplicity, the α particles are treated as noninteracting Boltzmann particles in the present calculation. The surface and Coulomb energy densities are given by

$$
f_{\text{surf}} = \frac{D \tau u_{\text{in}}}{r_D},
\tag{3}
$$

$$
f_{\text{Coul}} = \frac{e^2}{2} (\delta n_c)^2 r_D^2 u_{\text{in}} \Phi(u_{\text{in}}),
\tag{4}
$$

with

$$
\Phi(u_{\text{in}}) = \begin{cases} \frac{1}{D+2}\left(\frac{2-Du_{\text{in}}^{1-2/D}}{D-2} + u_{\text{in}}\right), & D = 1, 3 \\ \frac{u_{\text{in}} - 1 - \ln u_{\text{in}}}{D+2}, & D = 2. \end{cases} \tag{5}
$$

Here, τ denotes the surface tension, while $D = 1, 2, 3$ is the geometric dimension of the cell with r_D being the size of the inner part. u_{in} represents the volume fraction of the inner part, i.e., $u_{\text{in}} = u$ for droplet, rod, and slab configurations, and $u_{\text{in}} = 1 - u$ for tube and bubble configurations. $e = \sqrt{4\pi/137}$ is the electromagnetic coupling constant. $\delta n_c = n_p^L - (n_p^G + 2n_\alpha^G)$ is the charge-density difference between the liquid and gas phases. The surface tension τ is calculated by using the Thomas-Fermi approach for a one-dimensional nuclear system with the same RMF parametrization [6,28]. At finite temperature, both the surface energy and surface entropy are included in the surface tension τ. It was shown in Ref. [68] that τ decreases with increasing temperature and decreasing proton fraction of the liquid phase. Meanwhile, it has also been reported that the model with a small slope parameter L leads to a large surface tension [28,29,43].

With given average density n_b and proton fraction Y_p, the free energy density f in Eq. (2) is considered a function of seven variables: $n_p^L, n_n^L, n_p^G, n_n^G, n_\alpha^G, u,$ and r_D. These variables satisfy the constraints of the proton and neutron number conservation, which can be expressed as

$$
u n_p^L + (1 - u)(n_p^G + 2n_\alpha^G) = n_b Y_p, \tag{6}
$$

$$
u n_n^L + (1 - u)(n_n^G + 2n_\alpha^G) = n_b(1 - Y_p). \tag{7}
$$

In order to derive the phase equilibrium conditions by minimizing the free energy density, we introduce the Lagrange multipliers μ_p and μ_n for the constraints, and then perform the minimization for the function,

$$
w = f - \mu_p\left[u n_p^L + (1 - u)(n_p^G + 2n_\alpha^G)\right]
$$
$$
- \mu_n\left[u n_n^L + (1 - u)(n_n^G + 2n_\alpha^G)\right]. \tag{8}
$$

By minimizing w with respect to the variables, we obtain the following relations:

$$
0 = \frac{\partial w}{\partial n_n^L} = u\left[\mu_n^L - \mu_n\right], \tag{9}
$$

$$
0 = \frac{\partial w}{\partial n_n^G} = (1 - u)\left[\mu_n^G - \mu_n\right], \tag{10}
$$

$$
0 = \frac{\partial w}{\partial n_p^L} = u\left[\mu_p^L - \mu_p\right] + \frac{2f_{\text{Coul}}}{\delta n_c}, \tag{11}
$$

$$
0 = \frac{\partial w}{\partial n_p^G} = (1 - u)\left[\mu_p^G - \mu_p\right] - \frac{2f_{\text{Coul}}}{\delta n_c}, \tag{12}
$$

$$
0 = \frac{\partial w}{\partial n_\alpha^G} = (1 - u)\left[\mu_\alpha^G - 2(\mu_p + \mu_n)\right] - \frac{4f_{\text{Coul}}}{\delta n_c}, \tag{13}
$$

$$
0 = \frac{\partial w}{\partial u} = \left[f^L - \mu_p n_p^L - \mu_n n_n^L\right]
$$
$$
- \left[f^G - \mu_p\left(n_p^G + 2n_\alpha^G\right) - \mu_n\left(n_n^G + 2n_\alpha^G\right)\right]
$$
$$
\pm \left[\frac{f_{\text{surf}}}{u_{\text{in}}} + \frac{f_{\text{Coul}}}{u_{\text{in}}}\left(1 + u_{\text{in}}\frac{\Phi'}{\Phi}\right)\right], \tag{14}
$$

$$
0 = \frac{\partial w}{\partial r_D} = -\frac{f_{\text{surf}}}{r_D} + \frac{2f_{\text{Coul}}}{r_D}. \tag{15}
$$

According to Eqs. (9)–(13), the equilibrium conditions for chemical potentials are written as

$$
\mu_n^G = \mu_n^L, \tag{16}
$$

$$
\mu_p^G = \mu_p^L + \frac{2f_{\text{Coul}}}{u(1 - u)\delta n_c}, \tag{17}
$$

$$
\mu_\alpha^G = 2\mu_p^G + 2\mu_n^G. \tag{18}
$$

The equilibrium condition for the pressures between the liquid and gas phases is achieved from Eq. (14) and written as

$$
P^G = P^L + \frac{2f_{\text{Coul}}}{\delta n_c}\left(\frac{n_p^L}{u} + \frac{n_p^G + 2n_\alpha^G}{1 - u}\right)
$$
$$
\mp \frac{f_{\text{Coul}}}{u_{\text{in}}}\left(3 + u_{\text{in}}\frac{\Phi'}{\Phi}\right), \tag{19}
$$

where the sign of the last term is "−" for droplet, rod, and slab configurations, or "+" for tube and bubble configurations. It is clear that equilibrium conditions for two-phase coexistence are altered due to the inclusion of surface and Coulomb terms in the minimization procedure and, as a result, they are different from the Gibbs equilibrium conditions. Compared to the Gibbs conditions with equal pressures and chemical potentials between the two phases, the additional terms in Eqs. (17) and (19) are caused by the surface and Coulomb contributions. If we neglect the finite-size effects by taking the limit $\tau \to 0$, these additional terms disappear and the equilibrium equations would reduce to the Gibbs conditions. Based on the equilibrium condition $f_{\text{surf}} = 2f_{\text{Coul}}$ from Eq. (15), the size of the inner phase and that of the Wigner-Seitz cell are respectively given by

$$
r_D = \left[\frac{\tau D}{e^2(\delta n_c)^2 \Phi}\right]^{1/3}, \tag{20}
$$

$$
r_C = u_{\text{in}}^{-1/D} r_D. \tag{21}
$$

At given temperature T, average baryon density n_b, and proton fraction Y_p, we solve the equilibrium conditions together with the coupled equations of the RMF model in the liquid and gas phases for all pasta shapes, and then determine the thermodynamically stable state that has the lowest free energy density. In the pasta phases, the pressure and chemical potentials of the system may be different from those in the liquid and gas phases. Therefore, we compute these quantities
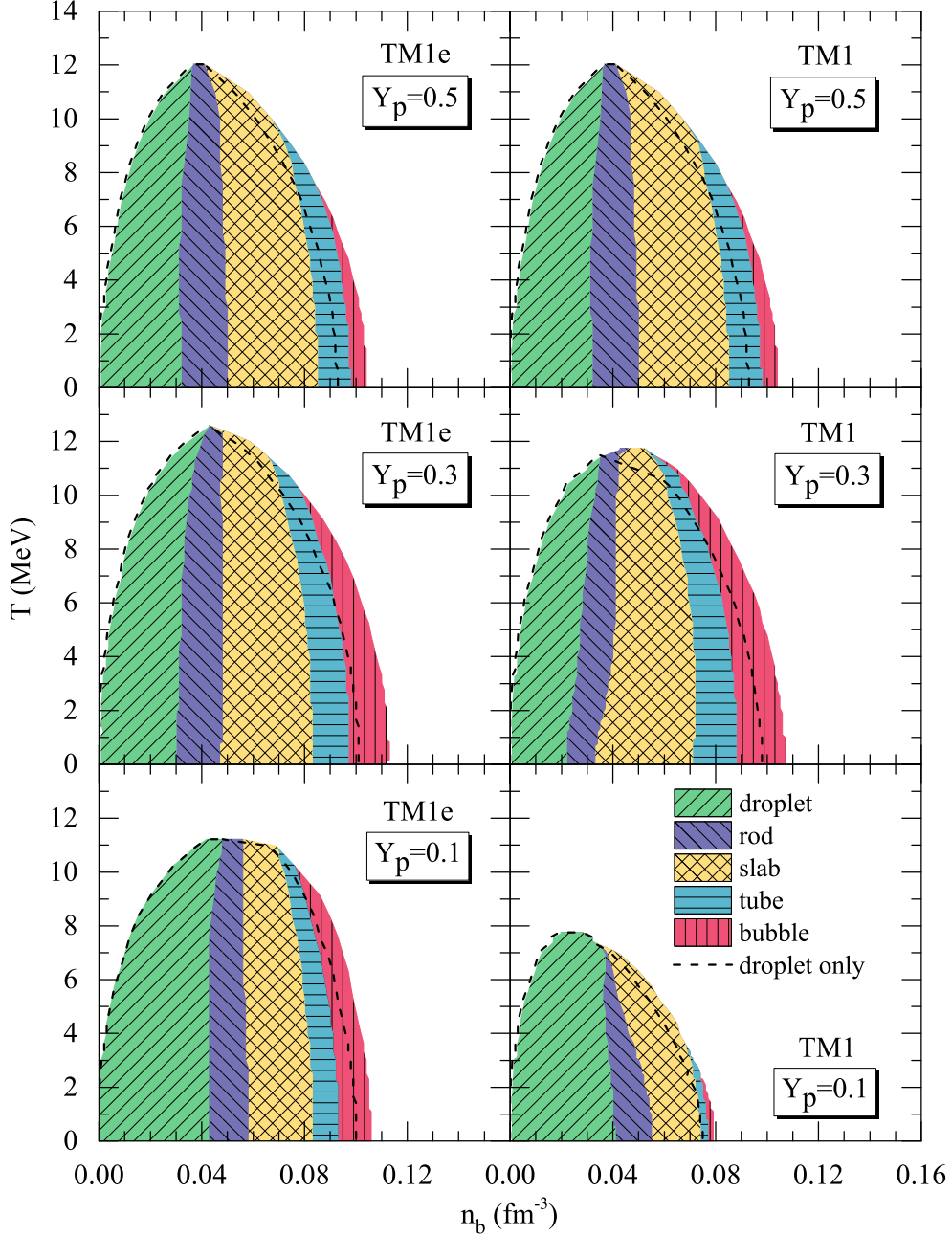
FIG. 1. Phase diagrams in the n_b-T plane for $Y_p = 0.1$, 0.3, and 0.5 obtained using the TM1e and TM1 models. Different colors indicate the regions for different pasta shapes. The boundary of nonuniform matter with only droplet configuration is shown by the dashed line for comparison.

by the thermodynamic relations

$$P = \left[n_b^2 \frac{\partial f(T, Y_p, n_b)/n_b}{\partial n_b} \right]_{T, Y_p}, \quad (22)$$

$$\mu_p = \left[\frac{\partial f(T, Y_p, n_b)}{\partial n_p} \right]_{T, n_n}, \quad (23)$$

$$\mu_n = \left[\frac{\partial f(T, Y_p, n_b)}{\partial n_n} \right]_{T, n_p}, \quad (24)$$

where $n_p = Y_p n_b$ and $n_n = (1 - Y_p)n_b$ are the average number densities of protons and neutrons, respectively.

III. RESULTS AND DISCUSSION

We explore the properties of nuclear pasta and its influence on the EOS for astrophysical simulations. The pasta phases are calculated in the CLD model, where a nuclear liquid coexists with a dilute gas consisting of free nucleons and α particles employing a sharp interface. For the nuclear interaction, we employ the TM1e model with a small symmetry
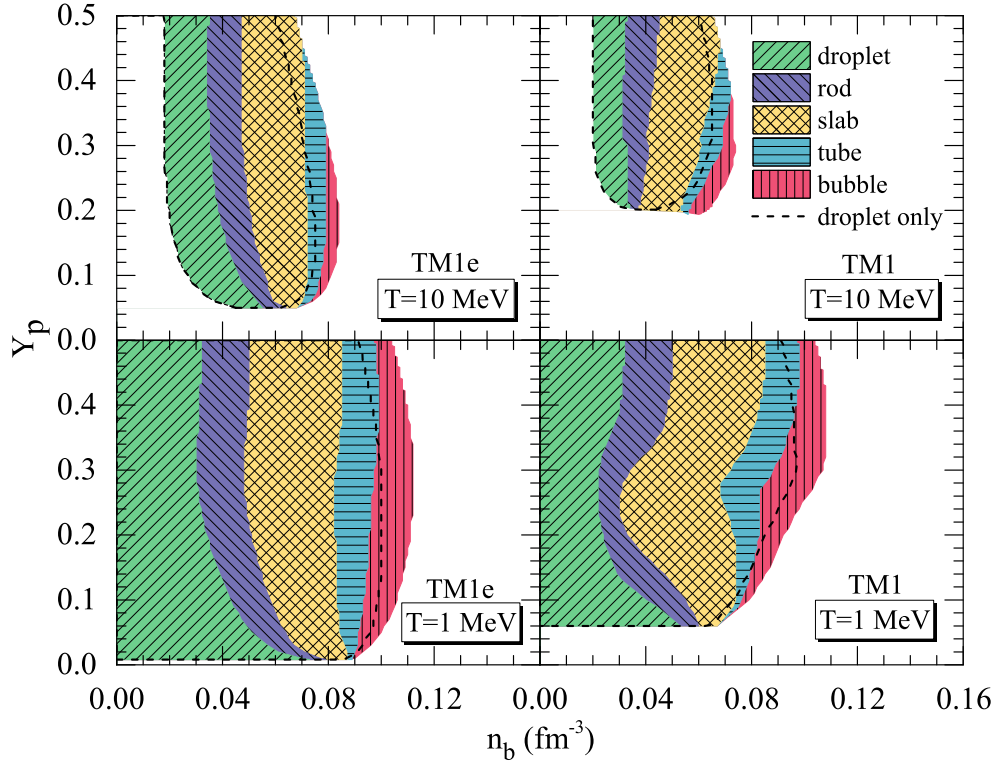
FIG. 2. Phase diagrams in the n_b-Y_p plane at $T = 1$ and 10 MeV obtained using the TM1e and TM1 models. Different colors indicate the regions for different pasta shapes. The boundary of nonuniform matter with only droplet configuration is shown by the dashed line for comparison.
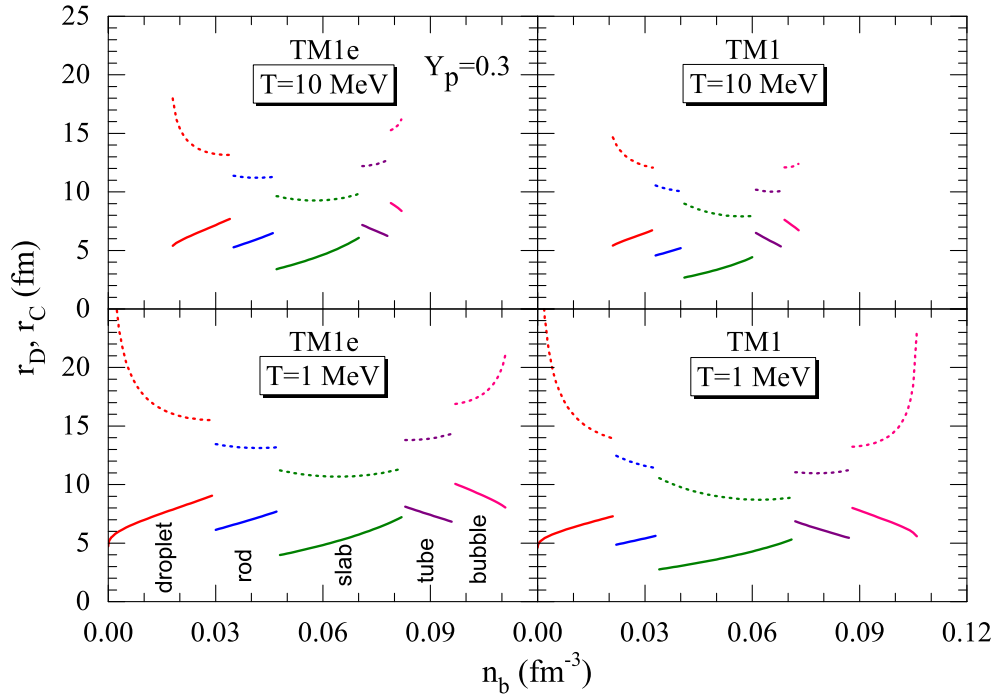

FIG. 3. Size of the nuclear pasta, r_D (solid lines), and that of the Wigner-Seitz cell, r_C (dotted lines), as a function of the baryon density n_b obtained using the TM1e and TM1 models. The results for $Y_p = 0.3$ at $T = 1$ and 10 MeV are shown in the lower and upper panels, respectively.
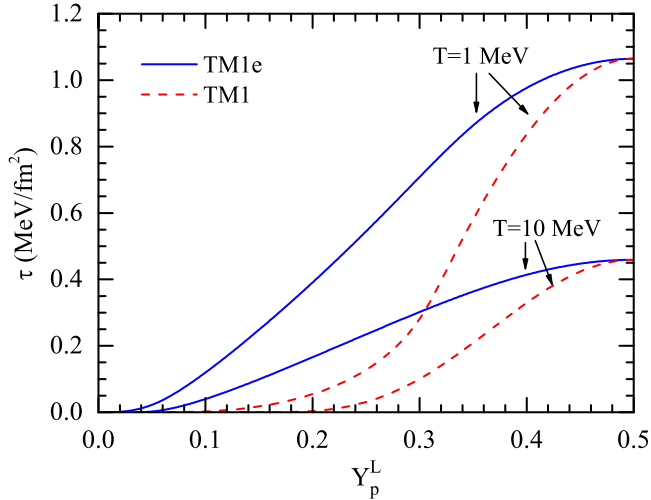
FIG. 4. Surface tension, τ, as a function of the proton fraction in the liquid phase, Y_p^L, at $T = 1$ and 10 MeV. The results are calculated from the Thomas-Fermi approach for a one-dimensional nuclear system using the TM1e and TM1 models.

energy slope $L = 40$ MeV, which is compatible with both experimental nuclear data and recent observations of neutron stars. To evaluate the effects of nuclear symmetry energy on the pasta phases, we compare the results of TM1e to those of the original TM1 model with a large symmetry energy slope $L = 110.8$ MeV. The difference between the TM1e and TM1 models is only in the isovector part, while the isoscalar properties in the two models remain the same.

We first discuss the phase diagram of hot and dense matter including nuclear pasta. At given temperature T, proton fraction Y_p, and baryon number density n_b, we perform calculations for all pasta phases, and then determine the most stable shape among them with the lowest free energy density. The transition to uniform matter occurs at a density of n_t where the free energy density of homogeneous matter becomes lower than that of pasta phases. In Fig. 1, we show the phase diagrams in the n_b-T plane for $Y_p = 0.1$, 0.3, and 0.5 obtained in the TM1e model (left panels) compared to that in the TM1 model (right panels). The results with only droplet configuration are plotted by the dashed lines, so that the influence of nuclear pasta on the phase diagram can
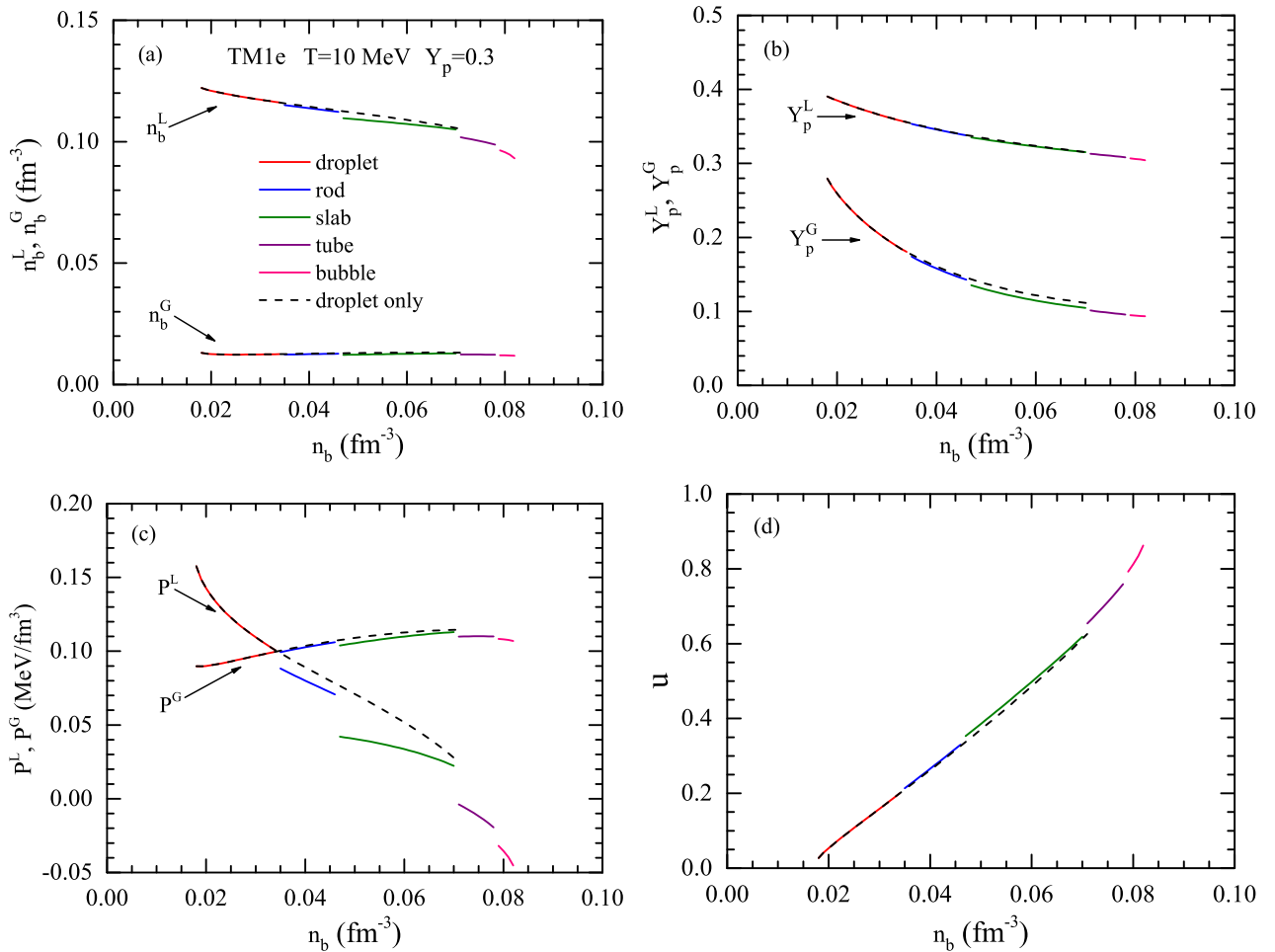

FIG. 5. Properties of the pasta phases at $T = 10$ MeV and $Y_p = 0.3$ using the TM1e model. The (a) coexisting liquid and gas densities n_b^L and n_b^G, (b) proton fractions Y_p^L and Y_p^G, (c) pressures P^L and P^G, and (d) volume fraction of the liquid phase, u, are plotted as a function of the average baryon density n_b.

be estimated. It is found that the inclusion of pasta phases
delays the transition to uniform matter. This is because the
configuration space is enlarged by considering nonspherical
nuclei in addition to the droplet. One can see that the density
range of nonuniform matter depends on both T and Y_p. At
low temperatures, various pasta shapes appear one by one
with increasing density, and the transition between different
shapes is only weakly dependent on T. As the temperature
increases, the density range of nonuniform matter shrinks,
while some pasta shapes like bubble and tube may not occur
before the transition to uniform matter. Eventually, the tem-
perature reaches the critical value T_c where the nonuniform
matter phase disappears completely; i.e., nuclear pasta cannot
be formed at $T > T_c$. Clearly, the critical temperature T_c for
$Y_p = 0.1$ obtained in the TM1 model is much smaller than
in other cases. This is because the TM1 model has a rather
large symmetry energy slope $L = 110.8$ MeV and a large L
is generally correlated to a small crust-core transition density
in neutron stars [9]. By comparing the results of the TM1e
model (left panels) to those of the TM1 model (right panels),
one can see the influence of the symmetry energy slope on
the phase diagram. There is almost no difference in the case
of $Y_p = 0.5$ and the difference for $Y_p = 0.3$ is still small.
However, a significant difference between the TM1e and TM1
models is observed in the case of $Y_p = 0.1$. This is because the
two models have the same isoscalar properties but different
symmetry energy behavior. It is well known that the symmetry
energy plays an important role in neutron-rich matter, but
it has no impact on the properties of symmetric nuclear
matter. A similar effect of the symmetry energy slope on
the phase diagram was also reported in Refs. [18,52], where
the parametrized Thomas-Fermi approximation was used and
only spherical nuclei were taken into account. In Fig. 2, we
show the phase diagrams in the n_b-Y_p plane for $T = 1$ and
10 MeV obtained in the TM1e and TM1 models. It is seen
that the onset of various pasta shapes is somewhat dependent
on Y_p. There are significant differences between the TM1e
and TM1 models in the low-Y_p region, where the behavior of
symmetry energy plays a crucial role. It is found that nuclear
pasta cannot be formed in the TM1 model for $Y_p < 0.2$ at
$T = 10$ MeV, whereas it exists until $Y_p \approx 0.05$ in the TM1e
model. At $T = 1$ MeV, the region of nuclear pasta extends to
a lower value of Y_p compared to the case of $T = 10$ MeV.

It is interesting to investigate the properties of nuclear pasta
appearing in nonuniform matter. We show in Fig. 3 the size
of the nuclear pasta (r_D) and that of the Wigner-Seitz cell
(r_C) as a function of the baryon density n_b. The results of the
TM1e model (left panels) for $Y_p = 0.3$ at $T = 1$ and 10 MeV
are compared to those obtained in the TM1 model (right
panels). It is observed that r_D in the droplet, rod, and slab
phases increases with increasing n_b, whereas r_D in the tube
and bubble phases decreases. This is related to an increase
of the volume fraction of the liquid phase. There are obvious
discontinuities in r_D and r_C at the transition between different
pasta shapes, which exhibit the character of the first-order
transition. Comparing the results between the TM1e and TM1
models, the tendencies of r_D and r_C are very similar in the two
models. It is noticed that the value of r_D in the TM1e model is
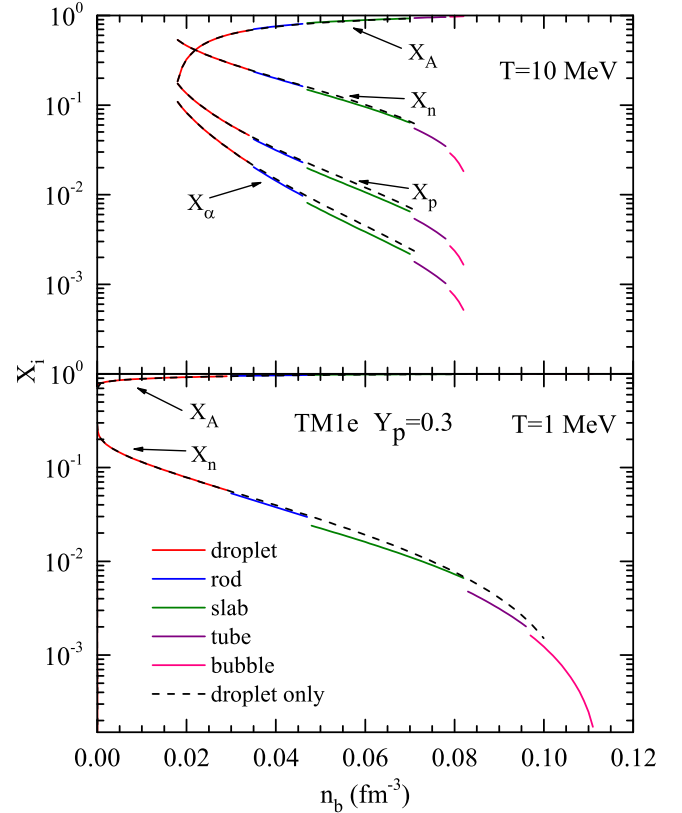slightly larger than that in the TM1 model. This is mainly due

FIG. 6. Fractions of neutrons (X_n), protons (X_p), α particles (X_α),
and heavy nuclei (X_A) as a function of the average baryon density
n_b in nonuniform matter for $Y_p = 0.3$ at $T = 1$ and 10 MeV using
the TM1e model. The results with nuclear pasta (solid lines) are
compared to those with droplet only (dashed lines).

to the difference of the surface tension τ, which is displayed
in Fig. 4. According to Eq. (20), a large surface tension τ
generally leads to a large nuclear size r_D. From Fig. 4, we can
see that the TM1e model with a small symmetry energy slope
$L = 40$ MeV predicts much larger surface tension than the
TM1 model with $L = 110.8$ MeV. The correlation between
the slope L and the surface tension τ has also been discussed
in Refs. [29,43,68].

In Fig. 5, we present several properties of nuclear pasta
described in the CLD model, where the liquid phase with
density n_b^L and proton fraction Y_p^L coexists with the gas phase
with n_b^G and Y_p^G. The equilibrium conditions for two-phase
coexistence are given by Eqs. (16)–(19). We plot in Fig. 5
the following quantities as a function of the average baryon
density n_b: the coexisting liquid and gas densities n_b^L and n_b^G
[Fig. 5(a)], proton fractions Y_p^L and Y_p^G [Fig. 5(b)], pressures
P^L and P^G [Fig. 5(c)], and volume fraction of the liquid
phase u [Fig. 5(d)]. The calculations are performed at $T =
10$ MeV and $Y_p = 0.3$ with the TM1e model. To explore the
differences between spherical and nonspherical nuclei, we
show the results with only droplet configuration by the dashed
lines. It is found that the differences between pasta phases
and droplet configuration are rather small in Figs. 5(a), 5(b),
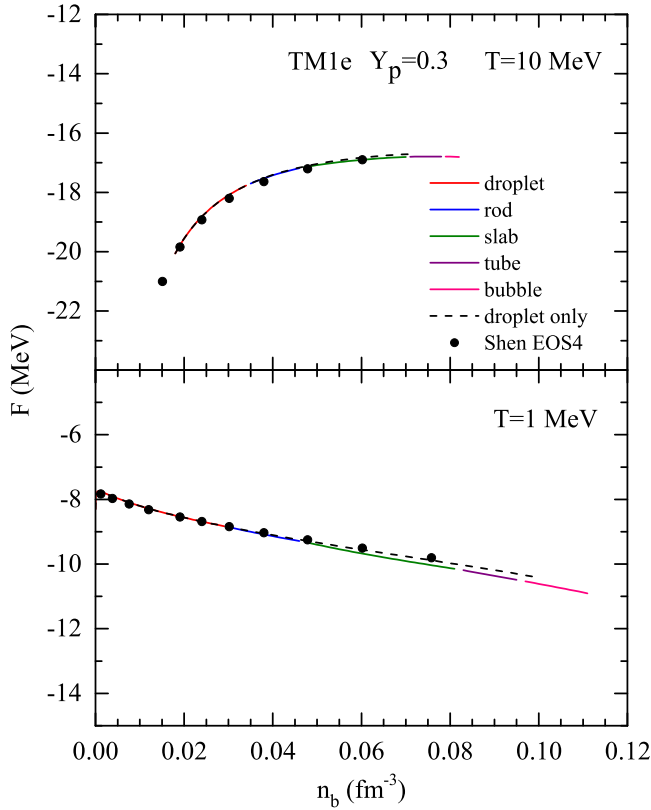and 5(d), whereas considerable differences are observed in

FIG. 7. Free energy per baryon F as a function of the baryon density n_b for $Y_p = 0.3$ at $T = 1$ and 10 MeV using the TM1e model. The results with nuclear pasta (solid lines) are compared to those with droplet only (dashed lines). The dots represent the values from the Shen EOS4 [52], which are calculated by a parameterized Thomas–Fermi approximation.

FIG. 8. Same as Fig. 7, but for pressure P.

the pressure of Fig. 5(c). Since the surface and Coulomb contributions are distinguished for different pasta shapes, it leads to the jumps at the transition between pasta shapes. It is noticeable that the pressure of the liquid phase (P^L) is clearly different from that of the gas phase (P^G), which is due to the surface and Coulomb contributions given by the last two terms in Eq. (19). On the contrary, the coexisting liquid and gas phases have equal pressures according to the Gibbs equilibrium conditions used in the CP method. In Fig. 5(b), the proton fraction Y_p^L decreases with increasing n_b, which implies that heavy nuclei become more neutron rich before dissolving into uniform matter. The volume fraction of the liquid phase u shown in Fig. 5(d) increases monotonically and nonspherical nuclei appear at $u \approx 0.21$. A simple estimate based on the Bohr-Wheeler fission condition indicates that a spherical nucleus becomes unstable to quadrupolar deformation at $u > 1/8$ [74]. In the CP method, the transition from droplet to rod occurs at $u \approx 0.22$, which is very close to the value obtained in the present calculation using the CLD method.

We display in Fig. 6 the fractions of neutrons, protons, α particles, and heavy nuclei as a function of the average baryon density n_b in nonuniform matter for $Y_p = 0.3$ at $T = 1$ and 10 MeV. These quantities are calculated in the CLD model
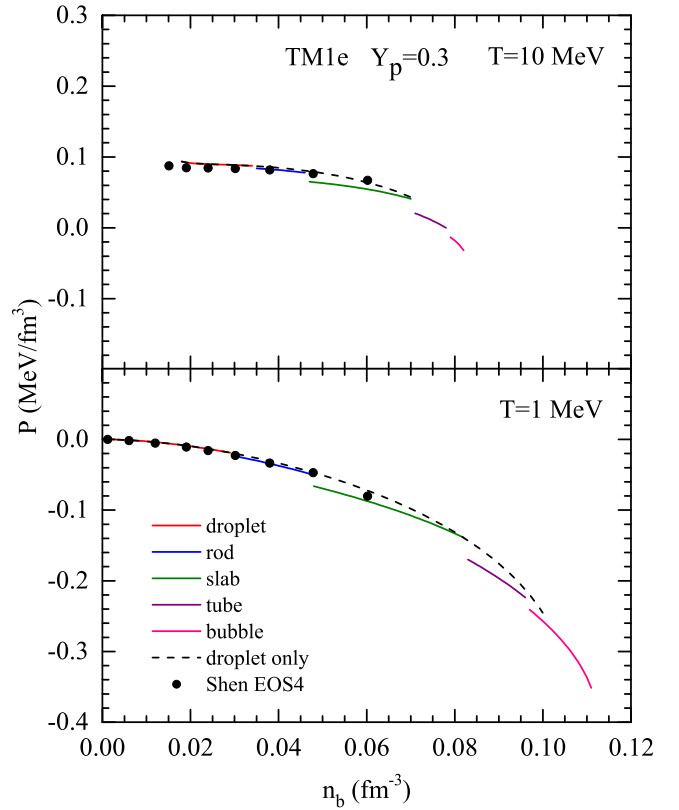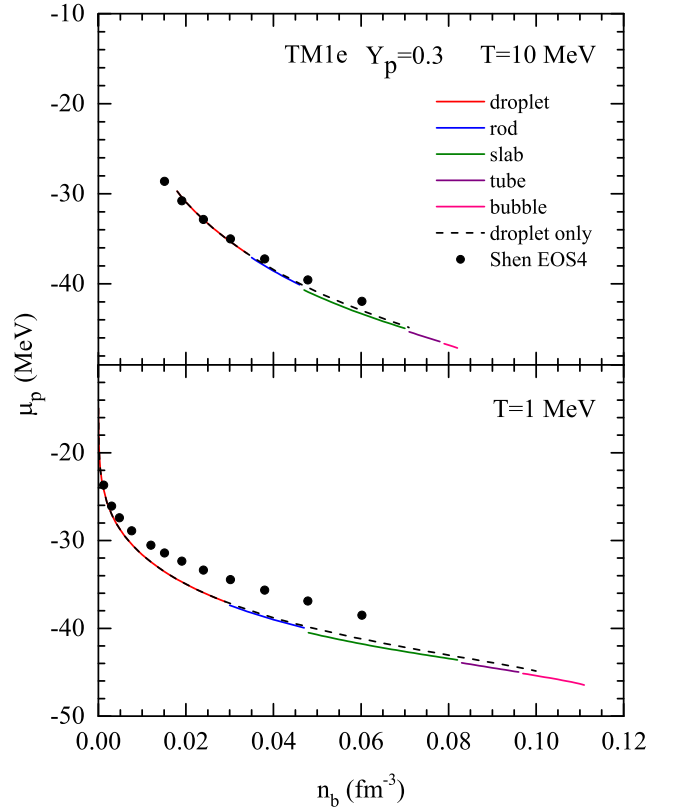
by $X_A = u(n_n^L + n_p^L)/n_b$, $X_\alpha = (1 - u)4n_\alpha^G/n_b$, and $X_i = (1 - u)n_i^G/n_b$ $(i = n, p)$. Compared to the results with only droplet configuration (dashed lines), the tendency of X_i with the inclusion of nuclear pasta is very similar, but small discontinuities appear at the change of pasta shapes. In the case of $T = 10$ MeV (upper panel), there are noticeable fractions of protons (X_p) and α particles (X_α), which are reduced to almost zero at $T = 1$ MeV (lower panel). Moreover, the fraction of heavy nuclei (X_A) is dominant in nonuniform matter and the value of X_A at $T = 10$ MeV is smaller than that at $T = 1$ MeV. This is because, at higher temperature, the particle densities in the gas phase are significantly enhanced, whereas the densities in the liquid phase are insensitive to the temperature due to their high degeneracy. We can see that X_n, X_p, and X_α decrease with increasing n_b, which is related to the increase of the volume fraction u shown in Fig. 5(d).

It is essential to analyze the influence of nuclear pasta on the thermodynamic quantities which play crucial roles in numerical simulations of core-collapse supernovas and neutron-star mergers. It is also important to compare the present results in the CLD model to those from a realistic EOS table with the same nuclear interaction, so that the uncertainty due to different descriptions of nonuniform matter can be estimated. In Fig. 7, we show the free energy per baryon, F, as a function of the baryon density n_b for $Y_p = 0.3$ at $T = 1$ and 10 MeV. The results with the inclusion of nuclear pasta (solid lines) are slightly smaller than those with droplet only (dashed lines) due to the enlargement of
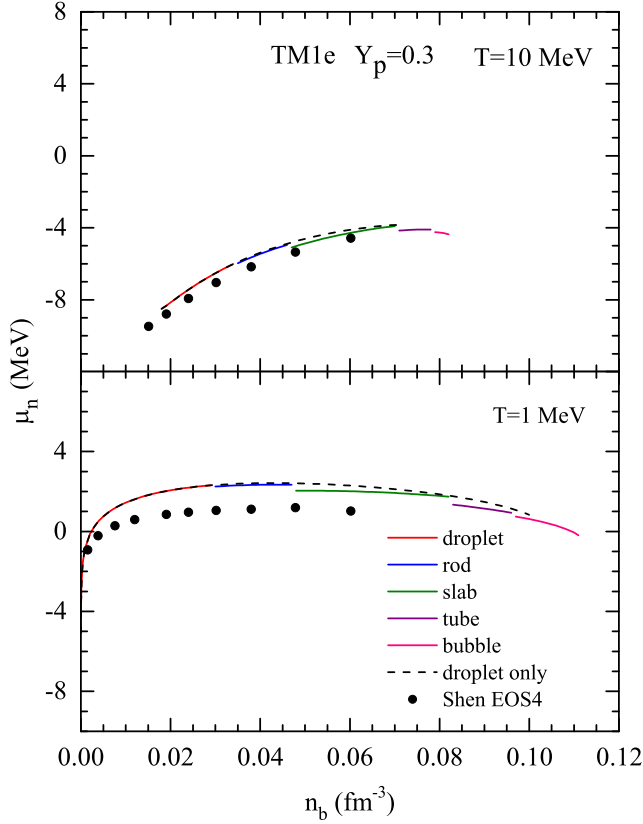
FIG. 9. Same as Fig. 7, but for chemical potential of neutrons, μ_n.

FIG. 10. Same as Fig. 7, but for chemical potential of protons, μ_p.

the configuration space by considering nonspherical nuclei. Meanwhile, the results from the realistic Shen EOS4 [52], which were constructed using a parametrized Thomas-Fermi approximation with the TM1e model, are shown by dots for comparison. It is found that the values of F taken from the Shen EOS4 are very close to the present results obtained using the CLD method. This confirms that the two methods are consistent with each other for calculating the free energies. We see that F increases with the density in the case of $T = 10$ MeV (upper panel), while it decreases at $T = 1$ MeV (lower panel). This is because $F = E - TS$ is related to the behaviors of the internal energy E and the entropy S. As the density increases, the entropy per baryon, S, decreases (see, e.g., Fig. 11 of Ref. [52]), which leads to the increase of F at higher temperature. On the contrary, the entropy plays less of a role at lower temperature, where the decrease of internal energy E is dominant. In Fig. 8, we display the pressure P as a function of the baryon density n_b for $Y_p = 0.3$ at $T = 1$ and 10 MeV. Compared to the results with droplet only (dashed lines), small discontinuities are observed in the pressures with the inclusion of pasta phases (solid lines) due to the change of pasta shapes. The discontinuities exhibit the character of the first-order transition. It is found that the pressures taken from the Shen EOS4 are consistent with the present results obtained using the CLD method. Comparing the cases between $T = 1$ and 10 MeV, the pressure at higher temperature is relatively larger, while the tendencies of P in the two cases are very similar. We note that the result shown in Fig. 8 represents

the baryon pressure without contributions from electrons and photons. In fact, the pressure of nonuniform matter is dominated by the background electron gas, which ensures the total pressure is positive. Therefore, the influence of nuclear pasta on the pressure is neglectable. In Figs. 9 and 10, the chemical potentials of neutrons and protons, μ_n and μ_p, are shown as a function of the baryon density n_b for $Y_p = 0.3$ at $T = 1$ and 10 MeV. It is observed that the results with nuclear pasta (solid lines) are very close to those with droplet only (dashed lines), whereas the change of pasta shapes may cause small discontinuities in μ_n and μ_p. One can see that μ_p decreases with increasing n_b, which is related to the decrease of the proton density in the gas phase. There are visible differences between the present results of the CLD model and those from the Shen EOS4 obtained by a Thomas-Fermi calculation. This implies that the chemical potentials are relatively sensitive to the method used for describing nonuniform matter. Since the chemical potentials are calculated from the first derivative of the free energy as given in Eqs. (23) and (24), the differences in chemical potentials could be more obvious than those in the free energy. Furthermore, the chemical potentials, μ_n and μ_p, are sensitively dependent on the density distributions of protons and neutrons, which are clearly different between the CLD model and the parametrized Thomas-Fermi approximation. The relatively large differences in μ_p between the present results and those from the Shen EOS4 may be partly due to different treatments of the Coulomb contributions between the two methods. In the present calculation using the

CLD method, the Coulomb energy is related to the surface energy by the equilibrium condition $f_{surf} = 2f_{Coul}$, where the surface tension τ is determined self-consistently as described in Refs. [6,28]. In the parametrized Thomas-Fermi approximation used in the Shen EOS4, the Coulomb energy is related to a gradient parameter F_0, which is somewhat underestimated in comparison to the self-consistent Thomas-Fermi approximation [75]. Notable differences in μ_p were also found and discussed in Ref. [75]. Generally speaking, the inclusion of nuclear pasta does not lead to significant differences in the thermodynamic quantities, but it may be important for the neutrino scattering rates and elastic properties of stellar matter.

IV. CONCLUSIONS

In this work, we investigated the properties of nuclear pasta appearing in hot and dense matter, associated with core-collapse supernovas and neutron-star mergers. We employed the compressible liquid-drop (CLD) model to describe the pasta phases with various geometric shapes. In the CLD model, the matter in the Wigner-Seitz cell is assumed to separate into a dense liquid phase of nucleons and a dilute gas phase of nucleons and α particles by a sharp interface. The equilibrium conditions between the liquid and gas phases were derived by minimization of the total free energy including the surface and Coulomb contributions, which are clearly different from the Gibbs equilibrium conditions. For the nuclear interaction, we employed the TM1e model with a small symmetry energy slope $L = 40$ MeV, which could be compatible with both experimental nuclear data and recent observations of neutron stars. To evaluate the influence of the density dependence of symmetry energy, the results of the TM1e model were compared to those of the original TM1 model with a large symmetry energy slope $L = 110.8$ MeV. It is noteworthy that the TM1e and TM1 models have the same properties of symmetric nuclear matter but different density dependencies of symmetry energy, so that the comparison between the two models reflects the influence solely from the symmetry energy without interference of the isoscalar part.

At given temperature T, proton fraction Y_p, and average baryon density n_b, we performed calculations for all pasta phases considered, and then determined the thermodynamically stable state with the lowest free energy. The transition from nonuniform matter to uniform matter occurs at the density where the free energy density of pasta phases becomes higher than that of homogeneous matter. It was found that the inclusion of pasta phases could significantly delay the transition to uniform matter as compared to the case with spherical nuclei only. From the phase diagrams obtained, it was observed that at lower temperatures various pasta shapes appear one by one with increasing density and their density ranges are only weakly dependent on the temperature. At higher temperatures, the density ranges shrink and some pasta shapes may have no chance to appear before the transition to uniform matter. When the temperature reaches the critical value T_c, nuclear pasta cannot be formed and the nonuniform matter phase disappears completely. It was shown that the critical temperature T_c depends on both the proton fraction Y_p and the nuclear model used. Significant differences between the TM1e and TM1 models could be observed in the phase diagram at the low-Y_p region. This implies that nuclear symmetry energy and its density dependence play a crucial role in determining the properties of pasta phases in neutron-rich matter.

The present results with pasta phases using the CLD method were compared to those in the realistic EOS table for astrophysical simulations, where the parametrized Thomas-Fermi approximation was used and only spherical nuclei were taken into account. It was found that thermodynamic quantities obtained in the two methods are consistent with each other, but the inclusion of pasta phases causes small discontinuities at the change of pasta shapes. It is likely that the influence of pasta phases on the EOS for astrophysical simulations is relatively limited. The discontinuities of the first-order phase transition in pasta may play a role in the neutron-star cooling and affect the glitch phenomena. Possible impacts of nuclear pasta on the neutrino scattering rates need to be studied in future work.

[1] A. Burrows, Rev. Mod. Phys. **85**, 245 (2013).

[2] H.-T. Janka, Annu. Rev. Nucl. Part. Sci. **62**, 407 (2012).

[3] H.-T. Janka, T. Melson, and A. Summa, Annu. Rev. Nucl. Part. Sci. **66**, 341 (2016).

[4] H. Shen, H. Toki, K. Oyamatsu, and K. Sumiyoshi, Astrophys. J. Suppl. **197**, 20 (2011).

[5] H. Pais and J. R. Stone, Phys. Rev. Lett. **109**, 151101 (2012).

[6] S. S. Avancini, S. Chiacchiera, D. P. Menezes, and C. Providência, Phys. Rev. C **82**, 055807 (2010); **85**, 059904(E) (2012).

[7] G. Watanabe, H. Sonoda, T. Maruyama, K. Sato, K. Yasuoka, and T. Ebisuzaki, Phys. Rev. Lett. **103**, 121101 (2009).

[8] M. Okamoto, T. Maruyama, K. Yabana, and T. Tatsumi, Phys. Rev. C **88**, 025801 (2013).

[9] S. S. Bao and H. Shen, Phys. Rev. C **91**, 015807 (2015).

[10] M. E. Caplan, C. R. Forsman, and A. S. Schneider, arXiv:2005.04766.

[11] B. Schuetrumpf, M. A. Klatt, K. Iida, J. A. Maruhn, K. Mecke, and P.-G. Reinhard, Phys. Rev. C **87**, 055805 (2013).

[12] M. Oertel, M. Hempel, T. Klähn, and S. Typel, Rev. Mod. Phys. **89**, 015007 (2017).

[13] J. M. Lattimer and F. D. Swesty, Nucl. Phys. A **535**, 331 (1991).

[14] A. S. Schneider, L. F. Roberts, and C. D. Ott, Phys. Rev. C **96**, 065802 (2017).

[15] A. S. Schneider, C. Constantinou, B. Muccioli, and M. Prakash, Phys. Rev. C **100**, 025803 (2019).

[16] H. Shen, H. Toki, K. Oyamatsu, and K. Sumiyoshi, Nucl. Phys. A **637**, 435 (1998).

[17] H. Shen, H. Toki, K. Oyamatsu, and K. Sumiyoshi, Prog. Theor. Phys. **100**, 1013 (1998).

[18] H. Togashi, K. Nakazato, Y. Takehara, S. Yamamuro, H. Suzuki, and M. Takano, Nucl. Phys. A **961**, 78 (2017).

[19] A. Burrows and J. M. Lattimer, Astrophys. J. **285**, 294 (1984).

[20] M. Hempel and J. Schaffner-Bielich, Nucl. Phys. A **837**, 210 (2010).

[21] S. Furusawa, S. Yamada, K. Sumiyoshi, and H. Suzuki, Astrophys. J. **738**, 178 (2011).

[22] S. Furusawa, K. Sumiyoshi, S. Yamada, and H. Suzuki, Astrophys. J. **772**, 95 (2013).

[23] S. Furusawa, K. Sumiyoshi, S. Yamada, and H. Suzuki, Nucl. Phys. A **957**, 188 (2017).

[24] A. W. Steiner, M. Hempel, and T. Fischer, Astrophys. J. **774**, 17 (2013).

[25] D. G. Ravenhall, C. J. Pethick, and J. R. Wilson, Phys. Rev. Lett. **50**, 2066 (1983).

[26] M. Hashimoto, H. Seki, and M. Yamada, Prog. Theor. Phys. **71**, 320 (1984).

[27] G. Watanabe, K. Iida, and K. Sato, Nucl. Phys. A **676**, 455 (2000); **726**, 357 (2003).

[28] S. S. Bao and H. Shen, Phys. Rev. C **89**, 045807 (2014).

[29] K. Oyamatsu and K. Iida, Phys. Rev. C **75**, 015801 (2007).

[30] F. Grill, C. Providência, and S. S. Avancini, Phys. Rev. C **85**, 055808 (2012).

[31] H. Pais, S. Chiacchiera, and C. Providência, Phys. Rev. C **91**, 055801 (2015).

[32] R. D. Williams and S. E. Koonin, Nucl. Phys. A **435**, 844 (1985).

[33] M. Okamoto, T. Maruyama, K. Yabana, and T. Tatsumi, Phys. Lett. B **713**, 284 (2012).

[34] P. Magierski and P.-H. Heenen, Phys. Rev. C **65**, 045804 (2002).

[35] W. G. Newton and J. R. Stone, Phys. Rev. C **79**, 055801 (2009).

[36] I. Sagert, G. I. Fann, F. J. Fattoyev, S. Postnikov, and C. J. Horowitz, Phys. Rev. C **93**, 055801 (2016).

[37] F. J. Fattoyev, C. J. Horowitz, and B. Schuetrumpf, Phys. Rev. C **95**, 055804 (2017).

[38] M. E. Caplan and C. J. Horowitz, Rev. Mod. Phys. **89**, 041002 (2017).

[39] T. Maruyama, K. Niita, K. Oyamatsu, T. Maruyama, S. Chiba, and A. Iwamoto, Phys. Rev. C **57**, 655 (1998).

[40] H. Sonoda, G. Watanabe, K. Sato, K. Yasuoka, and T. Ebisuzaki, Phys. Rev. C **77**, 035806 (2008); **81**, 049902(E) (2010).

[41] A. S. Schneider, C. J. Horowitz, J. Hughto, and D. K. Berry, Phys. Rev. C **88**, 065807 (2013).

[42] A. S. Schneider, D. K. Berry, C. M. Briggs, M. E. Caplan, and C. J. Horowitz, Phys. Rev. C **90**, 055805 (2014).

[43] S. S. Avancini, C. C. Barros, Jr., L. Brito, S. Chiacchiera, D. P. Menezes, and C. Providência, Phys. Rev. C **85**, 035806 (2012).

[44] S. S. Bao, J. N. Hu, Z. W. Zhang, and H. Shen, Phys. Rev. C **90**, 045802 (2014).

[45] A. Roggero, J. Margueron, L. F. Roberts, and S. Reddy, Phys. Rev. C **97**, 045804 (2018).

[46] C. J. Horowitz, D. K. Berry, M. E. Caplan, T. Fischer, Z. Lin, W. G. Newton, E. O'Connor, and L. F. Roberts, arXiv:1611.10226.

[47] B. P. Abbott et al. (LIGO Scientific Collaboration and Virgo Collaboration), Phys. Rev. D **96**, 122006 (2017).

[48] C. J. Pethick, Z. W. Zhang, and D. N. Kobyakov, Phys. Rev. C **101**, 055802 (2020).

[49] C. J. Pethick, Acta Phys. Pol. B **50**, 2145 (2019).

[50] M. E. Caplan, A. S. Schneider, and C. J. Horowitz, Phys. Rev. Lett. **121**, 132701 (2018).

[51] Y. Sugahara and H. Toki, Nucl. Phys. A **579**, 557 (1994).

[52] H. Shen, F. Ji, J. N. Hu, and K. Sumiyoshi, Astrophys. J. **891**, 148 (2020).

[53] P. B. Demorest, T. Pennucci, S. M. Ranson, M. S. E. Roberts, and J. W. T. Hessels, Nature (London) **467**, 1081 (2010).

[54] E. Fonseca et al., Astrophys. J. **832**, 167 (2016).

[55] J. Antoniadis et al., Science **340**, 1233232 (2013).

[56] H. T. Cromartie et al., Nat. Astron. **4**, 72 (2020).

[57] B. P. Abbott et al. (LIGO Scientific Collaboration and Virgo Collaboration), Phys. Rev. Lett. **119**, 161101 (2017).

[58] B. P. Abbott et al. (LIGO Scientific Collaboration and Virgo Collaboration), Phys. Rev. Lett. **121**, 161101 (2018).

[59] I. Tews, J. Margueron, and S. Reddy, Phys. Rev. C **98**, 045804 (2018).

[60] Z. Y. Zhu, E. P. Zhou, and A. Li, Astrophys. J. **862**, 98 (2018).

[61] S. De, D. Finstad, J. M. Lattimer, D. A. Brown, E. Berger, and C. M. Biwer, Phys. Rev. Lett. **121**, 091102 (2018).

[62] F. J. Fattoyev, J. Piekarewicz, and C. J. Horowitz, Phys. Rev. Lett. **120**, 172702 (2018).

[63] T. Malik, N. Alam, M. Fortin, C. Providência, B. K. Agrawal, T. K. Jha, B. Kumar, and S. K. Patra, Phys. Rev. C **98**, 035804 (2018).

[64] B. P. Abbott et al. (LIGO Scientific Collaboration and Virgo Collaboration), Astrophys. J. Lett. **892**, L3 (2020).

[65] T. E. Riley et al., Astrophys. J. Lett. **887**, L21 (2019).

[66] M. C. Miller et al., Astrophys. J. Lett. **887**, L24 (2019).

[67] F. Ji, J. N. Hu, S. S. Bao, and H. Shen, Phys. Rev. C **100**, 045801 (2019).

[68] S. S. Bao and H. Shen, Phys. Rev. C **93**, 025807 (2016).

[69] C. J. Horowitz and J. Piekarewicz, Phys. Rev. Lett. **86**, 5647 (2001).

[70] J. Carriere, C. J. Horowitz, and J. Piekarewicz, Astrophys. J. **593**, 463 (2003).

[71] R. Cavagnoli, D. P. Menezes, and C. Providência, Phys. Rev. C **84**, 065810 (2011).

[72] C. Providência and A. Rabhi, Phys. Rev. C **87**, 055801 (2013).

[73] H. Pais and C. Providência, Phys. Rev. C **94**, 015808 (2016).

[74] C. J. Pethick and D. G. Ravenhall, Annu. Rev. Nucl. Part. Sci. **45**, 429 (1995).

[75] Z. W. Zhang and H. Shen, Astrophys. J. **788**, 185 (2014).